JACS
JOURNAL OF THE AMERICAN CHEMICAL SOCIETY

Article

pubs.acs.org/JACS

Electrochromic Bis(terpyridine)metal Complex Nanosheets

Kenji Takada, Ryota Sakamoto, Shi-Ting Yi, Shunsuke Katagiri, Tetsuya Kambe, and Hiroshi Nishihara*

Department of Chemistry, Graduate School of Science, The University of Tokyo, 7-3-1, Hongo, Bunkyo-ku, Tokyo 113-0033, Japan

Supporting Information

ABSTRACT: A series of electrochromic metal complex nanosheets comprising 1,3,5-tris(4-(2,2′:6′,2″-terpyridyl)phenyl)benzene or 1,3,5-tris((2,2′:6′,2″-terpyridyl)ethynyl)benzene and Fe^{2+} or Co^{2+} was synthesized. The preparation of multilayered nanosheets was achieved by liquid/liquid interfacial synthesis using an organic ligand solution and an aqueous metal−ion solution. The resultant nanosheet had a flat, smooth morphology and was several hundreds of nanometers thick. Upon its deposition on an indium tin oxide (ITO) electrode, the nanosheet underwent a reversible and robust redox reaction (Fe^{3+}/Fe^{2+} or Co^{2+}/Co^{+}) accompanied by a distinctive color change. Electrochromism was achieved in a solidified device composed of the nanosheet, a pair of ITO electrodes, and a polymer-supported electrolyte. The combination of Fe^{2+} and Co^{2+} nanosheets in one device—deposited on each ITO electrode—demonstrated dual-electrochromic behavior.

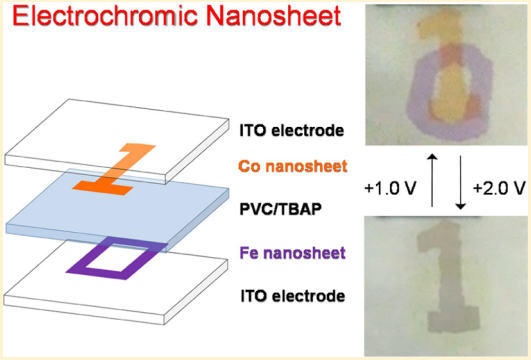

INTRODUCTION

The nanosheet is a new type of material that possesses a two-dimensional polymeric structure. The flagship nanosheet is graphene,[1−3] which has various fascinating properties such as an extensive and balanced carrier mobility. The success achieved with graphene encouraged researchers to investigate other nanosheet types including metal oxides,[4−8] metal sulfides,[9−12] and metal hydroxides.[13−17] These nanosheets are based on crystalline mother materials and are produced by mechanical or chemical exfoliation (i.e., top-down nanosheets).

Recently, nanosheets woven from molecular, atomic, and ionic components (i.e., bottom-up nanosheets) have been investigated extensively.[18−24] The greatest advantage of bottom-up over top-down nanosheets is that their structures and properties are tunable by design and choice of components. The attractive properties of bottom-up nanosheets have not yet been disclosed. We therefore designed and created the first conductive bottom-up nanosheet: a π-conjugated bis(dithiolene)nickel(II) complex nanosheet synthesized from benzenehexathiol as an organic ligand and nickel(II) ion as the metal center.[25]

Here we report on electrochromic bottom-up nanosheets: bis(terpyridine)iron(II) and cobalt(II) complex nanosheets (**1-Fe**, **2-Fe**, and **1-Co**) composed of three-fold symmetric terpyridine ligands 1,3,5-tris(4-(2,2′:6′,2″-terpyridyl)phenyl)benzene (**1**) or 1,3,5-tris((2,2′:6′,2″-terpyridyl)ethynyl)benzene (**2**) with Fe(II) or Co(II) ions (Figure 1). A pioneer work on this type of metal complex nanosheets was addressed by Schlüter and co-workers,[18−20] where synthetic and analytical progress was contributed. They realized and observed the single-layer two-dimensional polymers by means of air/liquid interfacial synthesis. Also, they found that the zinc(II) center was subject to transmetalation, giving rise to iron(II), cobalt(II), and lead(II) analogues. On the other hand, herein, we focus on the functionality of the bis(terpyridine)metal complex nanosheet. By taking advantage of the fast and robust redox activity of the bis(terpyridine)metal complex unit and also the porosity of the nanosheet structure, we demonstrate its quick and reversible electrochromic properties in solution and in a solidified device using multilayer nanosheets as active layers. Iron(II) and cobalt(II) complex nanosheets were placed on either side of a pair of transparent indium tin oxide (ITO) electrodes to form a dual-electrochromic device.

RESULTS AND DISCUSSION

To gain nanosheets with thicknesses suitable for the electrochromic application, **1-Fe** and **2-Fe** were prepared at the liquid/liquid interface between aqueous $Fe(BF_4)_2$ and a dichloromethane solution of **1** and **2**, respectively. After the two solutions were layered, thin purple films of **1-Fe** and **2-Fe** were generated at the interface as shown in Figures 2, panel a and 3, panel a. **1-Fe** and **2-Fe** were insoluble in any solvent, but they could be deposited easily onto flat substrates such as highly oriented pyrolytic graphite (HOPG), Si, and an ITO electrode. These features may be advantageous over molecular and soluble one-dimensional polymers, which, respectively, require chemical bonding and spin-coating in processing and also suffer from redissolution in media. Also, the enlargement of the size of the nanosheet was achieved using a larger container. Figure S1a of the Supporting Information shows **1-Fe** prepared in a container with a diameter of 90 mm.

Microscopic techniques provided information on the morphology of **1-Fe**. Transmission electron microscopy

Received: November 5, 2014
Published: March 19, 2015

DOI: 10.1021/ja510788b
J. Am. Chem. Soc. 2015, 137, 4681−4689

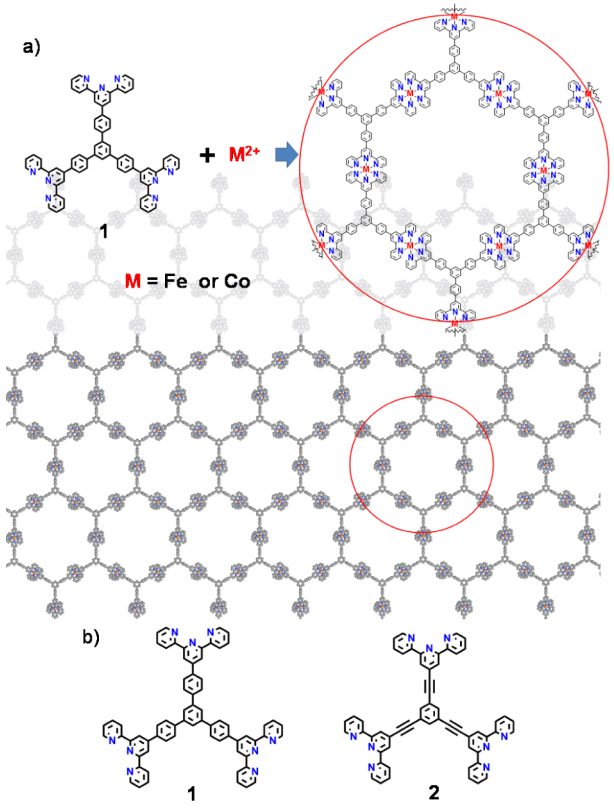

Figure 1. (a) Structure of bis(terpyridine)metal(II) complex nanosheets **1-Fe** and **1-Co**. (b) Chemical structures of ligands **1** and **2**.

(TEM) showed **1-Fe** to have a layered structure (Figure 2b), and scanning electron microscopy (SEM) showed a flat, sheet-like morphology (Figures 2c and S2). Atomic force microscopy (AFM) also revealed the flat surface of **1-Fe** (Figure 2d). From its cross-sectional analysis, the thickness of **1-Fe** was found to be approximately 200 nm. This corresponds to approximately 140 layers, considering the assumption proposed by Schlüter that a monolayer nanosheet is 1.4 nm thick.[18] Similarly, **2-Fe** has a flat surface with a thickness of approximately 300 nm (Figure 3b–d). The nanosheet thickness could be controlled by varying reaction conditions such as Fe(II) ion concentration and reaction time. For example, when dilute aqueous $Fe(BF_4)_2$ (5 mM) was used, **1-Fe** with a thickness of 9–10 nm (6–7 layers) was formed with a reaction time of 1 d (Figure S3a). Its AFM image features a uniform, smooth, and flat texture. In addition, a step-terrace structure is observed, where the upper layer also possesses a thickness of 9–10 nm. Therefore, this AFM image discloses the lamella structure of **1-Fe**. The extension of the reaction time to 5 d yielded 180 nm-thick **1-Fe** (corresponding to ca. 130 layers, Figure S3b).

The identification of **1-Fe** and **2-Fe** was conducted by X-ray photoelectron spectroscopy (XPS) and infrared (IR) spectroscopy. XP spectra of **1-Fe**, mononuclear Fe(II) complex $[Fe(tpy)_2](BF_4)_2{\cdot}H_2O$, (tpy: 2,2′:6′,2″-terpyridine), and ligand **1** with a focus on the N 1s, Fe 2p, B 1s, and F 1s core levels are shown in Figure 2, panel e. The N 1s peak derived from free ligand **1** at 397.5 eV shifted to 399.7 eV upon formation of the nanosheet. The new peak position is consistent with that of the corresponding mononuclear complex. Similarly, the binding energy of the Fe 2p core level of **1-Fe** was also equal to that of $[Fe(tpy)_2](BF_4)_2{\cdot}H_2O$ (Figure 2e). These results confirm that the complexation between **1** and Fe(II) ions is complete as far

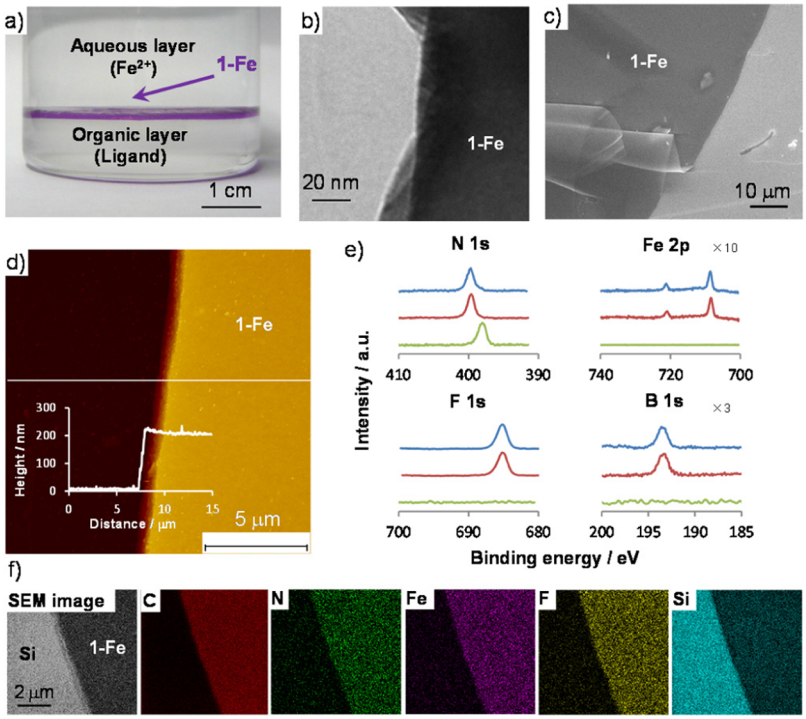

Figure 2. (a) **1-Fe** generated at the liquid/liquid interface between 25 mM aqueous $Fe(BF_4)_2$ and 0.1 mM **1** in CH_2Cl_2 after 24 h. (b) TEM image of **1-Fe**. (c) SEM image of **1-Fe** deposited on HOPG. (d) AFM image and its cross-section analysis of **1-Fe** on a Si substrate. (e) XP spectra of **1** (green), $[Fe(tpy)_2](BF_4)_2{\cdot}H_2O$ (red), and **1-Fe** (blue) focusing on N 1s, Fe 2p, F 1s, and B 1s core levels, respectively. The peak intensity is corrected using a standard sample, thereby being proportional to the element abundance. (f) SEM/EDS mapping of **1-Fe** for C, N, Fe, F, and Si.

DOI: 10.1021/ja510788b
J. Am. Chem. Soc. 2015, 137, 4681–4689

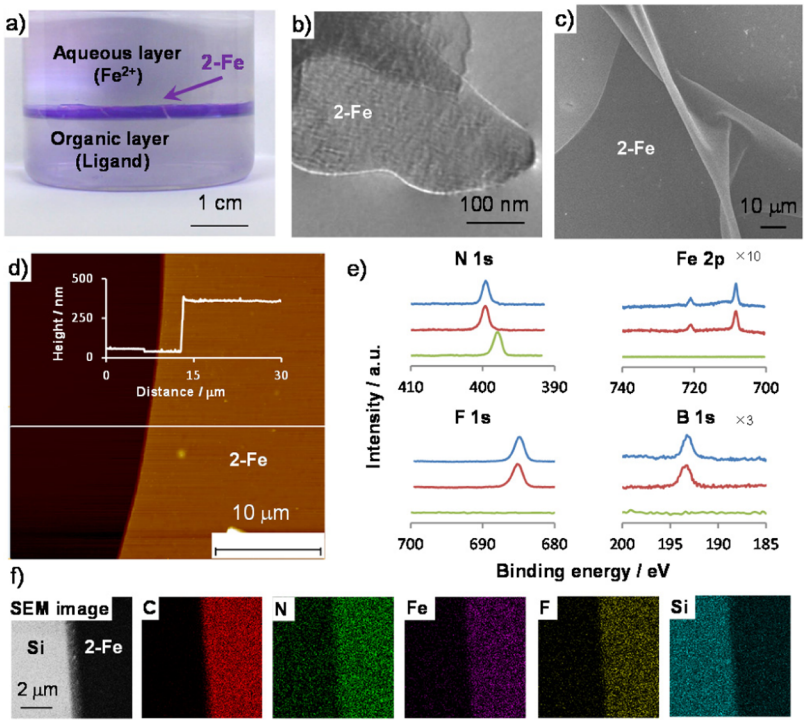

Figure 3. (a) **2-Fe** generated at the liquid/liquid interface between 25 mM aqueous $Fe(BF_4)_2$ and 0.12 mM **2** in CH_2Cl_2 after 24 h. (b) TEM image of **2-Fe**. (c) SEM image of **2-Fe** deposited on a Si substrate. (d) AFM image and its cross-section analysis of **2-Fe** on a Si substrate. (e) XP spectra of **2** (green), $[Fe(tpy)_2](BF_4)_2{\cdot}H_2O$ (red), and **2-Fe** (blue) focusing on the N 1s, Fe 2p, F 1s, and B 1s core levels, respectively. The peak intensity is corrected using a standard sample, thereby being proportional to the element abundance. (f) SEM/EDS mapping of **1-Fe** for C, N, Fe, F, and Si.

as the detection limit of XPS is concerned (0.1−1 atom %). The B 1s and F 1s peaks indicate the existence of BF_4^- as a counteranion. The peak positions of **2-Fe** in the XP spectrum are the same as those of **1-Fe** (Figure 3e). Element abundance was calculated using $[Fe(tpy)_2](BF_4)_2{\cdot}H_2O$ as a standard sample, giving N/Fe/F/B ratios of 6.05:1:8.36:1.97 and 6.02:1:8.64:1.92 for **1-Fe** and **2-Fe**, respectively. These ratios are in good agreement with the ideal value (N/Fe/F/B = 6:1:8:2) considering an error accompanying XPS (10%). In the IR spectrum of **1**, a C═C stretching vibration is visible at 1585 cm^{-1} (Figure S4). This peak shifted to higher wavenumbers in **1-Fe** and is visible at 1601 cm^{-1}. This is a typical change for a terpyridine ligand upon complexation to a metal ion.[26] Moreover, the broad absorption peak at approximately 1100 cm^{-1} is ascribed to BF_4^-. The IR spectrum of **2-Fe** shows characteristics similar to those of **1-Fe** (Figure S4). SEM with energy dispersive X-ray spectroscopy (SEM/EDS) mapping discloses that the constitutive elements of **1-Fe** and **2-Fe** (C, N, Fe, and F) are distributed homogeneously, while Si derived from the substrate is more conspicuous in the blank region (Figures 2f and 3f). We note that B K_α peak is hidden by the C K_α peak, such that mapping for B is not achieved. This series of data indicates that the nanosheet has a uniform sheet structure with the desired composition.

The mechanical strength of the multilayer nanosheet is good enough to be a self-standing film (Figure S5). Then we performed cyclic voltammetry for **1-Fe** and **2-Fe** physisorbed onto HOPG substrates (Figure 4a). One reversible redox wave was observed at $E^{0\prime}$ = 0.68 and 0.76 V versus Fc^+/Fc (Fc:ferrocene), respectively, when 1 M Bu_4NClO_4 in acetonitrile was used as an electrolyte solution. The redox reaction is assignable to the Fe^{3+}/Fe^{2+} couple of the $[Fe(tpy)_2]$ unit because these values are in good consistency with those of bis(terpyridine)iron(II) complex wires.[27−30] Because of the electron-withdrawing ability of the ethynylene linker, the Fe^{3+}/Fe^{2+} redox couple of **2-Fe** shifted in the anodic direction. Although both **1-Fe** and **2-Fe** were immobilized on HOPG, the anodic and cathodic peak currents, i_{pa} and i_{pc}, were not proportional to the scan rate ν, but to $\nu^{1/2}$ (Figure 4b). However, linear fits of the $i_{pa} - \nu^{1/2}$ and $i_{pc} - \nu^{1/2}$ plots do not cross the origin. This means that the redox reaction is not a simple diffusion-controlled process. In-plane redox conduction is one of the rate-determining steps, as we demonstrated for dendritic bis(terpyridine)iron(II) complex oligomer wires.[27,30]

This series of electrochemical activities is accompanied by a color change (e.g., electrochromism[31−33]). For example, Higuchi and co-workers reported on electrochromism using linear and branched bis(terpyridine)metal complex wires.[33] The UV−vis spectrum of **1-Fe** on an ITO electrode shows an absorption peak at λ_{max} = 578 nm, which can be attributed to a metal-to-ligand charge transfer (MLCT) band (Figure 4e). When **1-Fe** was oxidized electrochemically at 1.16 V, the MLCT band diminished and the color changed from deep purple to pale yellow (see Movie 1 in the Supporting Information and Figure 4d). When the oxidized nanosheet was reduced at 0.16 V, the MLCT band was revived (Figure S6), and the original color was reproduced.

To investigate the response time and durability of the electrochromism of **1-Fe**, potential-step chronoamperometry (PSCA) was conducted with UV−vis spectroscopic analysis. Figure 4, panel c shows an amperogram at an overpotential of +0.5 V (from 0.16−1.16 V). The faradaic current decays in 0.35 s (Figures 4c). This time scale is comparable to that of branched bis(terpyridine)iron(II) complex wires.[33] Figure 4, panel f shows the absorptivity at 578 nm during repetitive PSCA between 1.16 and 0.16 V. The absorption change was

DOI: 10.1021/ja510788b
J. Am. Chem. Soc. 2015, 137, 4681−4689

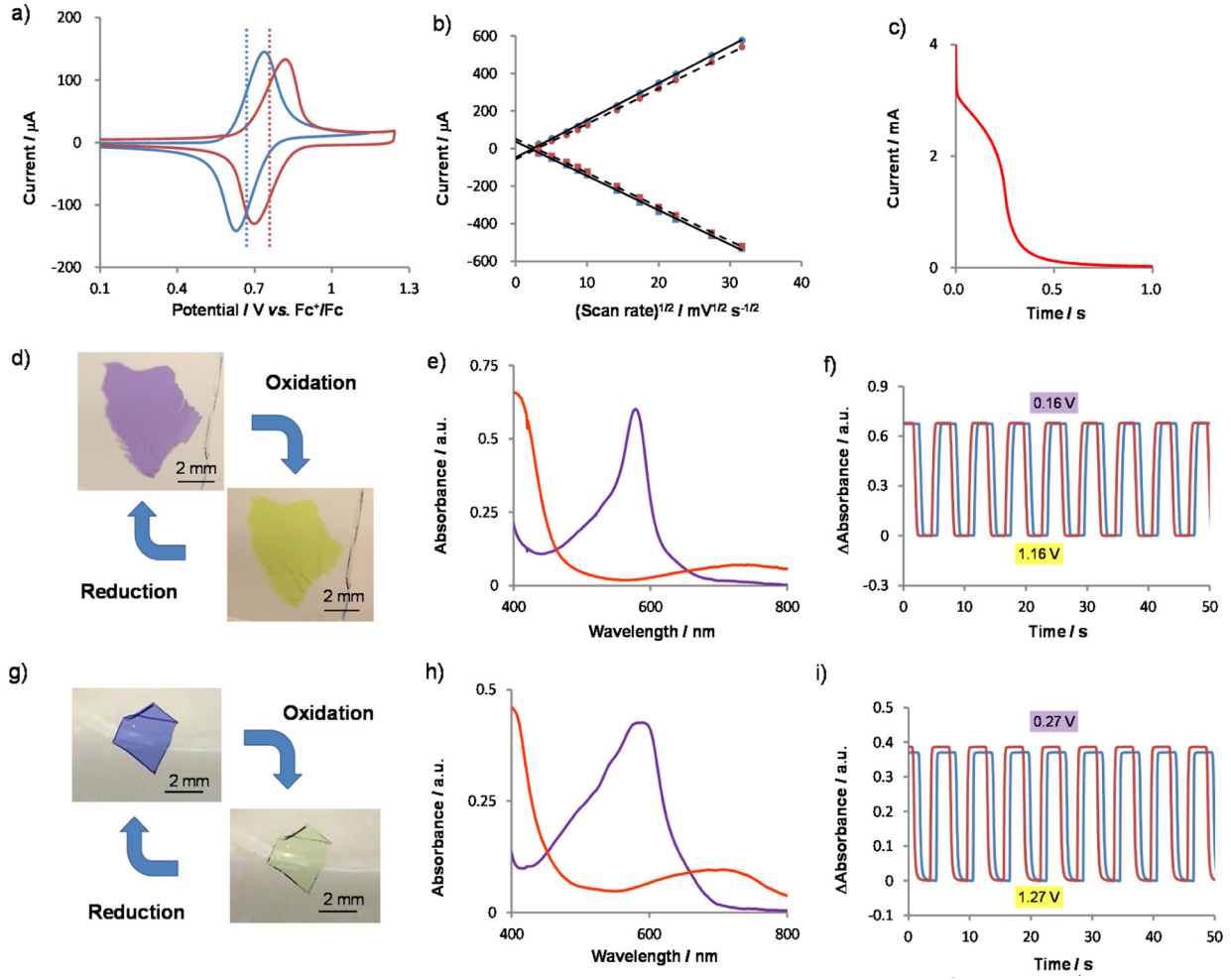

Figure 4. (a) Cyclic voltammograms of **1-Fe** (blue) and **2-Fe** (red) on HOPG in 1 M Bu_4NClO_4-MeCN solution (scan rate: 100 mV s^{-1}). The blue and red dotted lines represent formal potentials of the Fe^{3+}/Fe^{2+} couple. (b) $i_{pa} - v^{1/2}$ and $i_{pc} - v^{1/2}$ plots, where i_{pa} and i_{pc} denote anodic and cathodic peak currents, and v represents a scan rate. The blue solid circles and squares are derived from **1-Fe**, and the red ones are derived from **2-Fe**. The solid or dashed lines correspond to least-squares linear fits. (c) Chronoamperogram of **1-Fe** on an ITO electrode at an overpotential of +0.5 V (from 0.16−1.16 V). (d) Electrochromism of **1-Fe**. (e) UV−vis spectra of **1-Fe** (purple) and oxidized **1-Fe** (orange) on transparent ITO electrodes. (f) Change in the absorbance at 578 nm with repetitive PSCA between 1.16 and 0.16 V, corresponding to an overpotentials of +0.5 V and −0.5 V, respectively. Blue: from first to eighth cycles. Red: cycle 801st to 808th. Each potential was applied for 3 s. (g) Electrochromism of **2-Fe**. (h) UV−vis spectra of **2-Fe** (purple) and oxidized **2-Fe** (orange) on ITO electrodes. (i) Change in the absorbance at 590 nm with repetitive PSCA between 1.27 and 0.27 V, corresponding to an overpotentials of +0.5 V and −0.5 V, respectively. Blue: from first to eighth cycles. Red: cycle 1001st to 1008th. Each potential was applied for 3 s.

constant for at least 800 cycles, which indicates that the electrochromic behavior of **1-Fe** is durable.

The redox process of **2-Fe** was also accompanied by a color change from deep violet to pale yellow (Figure 4g and Movie 2 in the Supporting Information). UV−vis spectroscopy revealed that the MLCT peak at λ_{max} = 588 nm disappeared upon oxidation but reappeared after reduction (Figure 4h). The MLCT band of **2-Fe** shifted to 10 nm longer wavelengths than that of **1-Fe** because of the electron-withdrawing ethynylene linker. **2-Fe** also exhibited good durability over 1000 cycles and a fast response time (0.54 s) (Figures 4i and S7).

Electrochemical impedance spectroscopy (EIS) was conducted to gain kinetic information. A single ellipse was observed for both **1-Fe** and **2-Fe** (Figure S8). This is a typical feature for a surface-confined redox active species. The Randles circuit was used to determine the electron transfer rate constant k_{ET}, which was 678 and 398 s^{-1} for **1-Fe** and **2-Fe**, respectively. These values are greater than or comparable with those of bis(terpyridine)metal complex oligomer wires on gold electrodes (ca. 100 s^{-1}).[30]

Next, the use of cobalt(II) ions in the nanosheet system was examined. Ligand **1**, which provided a faster electron transfer, was used; **1-Co** was prepared by liquid/liquid interfacial synthesis. Aqueous $CoCl_2$ and a chloroform solution of **1** were used to form a bilayer. After the reaction system was kept still, a thin orange film formed at the interface (Figure 5a). The Co nanosheet morphology was observed by electron microscopy. TEM showed that **1-Co** had a layered sheet structure (Figure 5b). A flat nanosheet morphology was observed in SEM (Figure 5c). This series of observations supports the formation of the desired layered nanosheet, **1-Co**. From the AFM cross-sectional analysis (Figure 5d), we concluded that the **1-Co** was 120 nm thick, which corresponds to approximately 90 layers. Neither X-ray nor electron diffraction was again observed for **1-Co**, probably because of disorder in the location of the counteranion (Cl^-) or in the stacking of the nanosheet layers.

DOI: 10.1021/ja510788b
J. Am. Chem. Soc. 2015, 137, 4681−4689

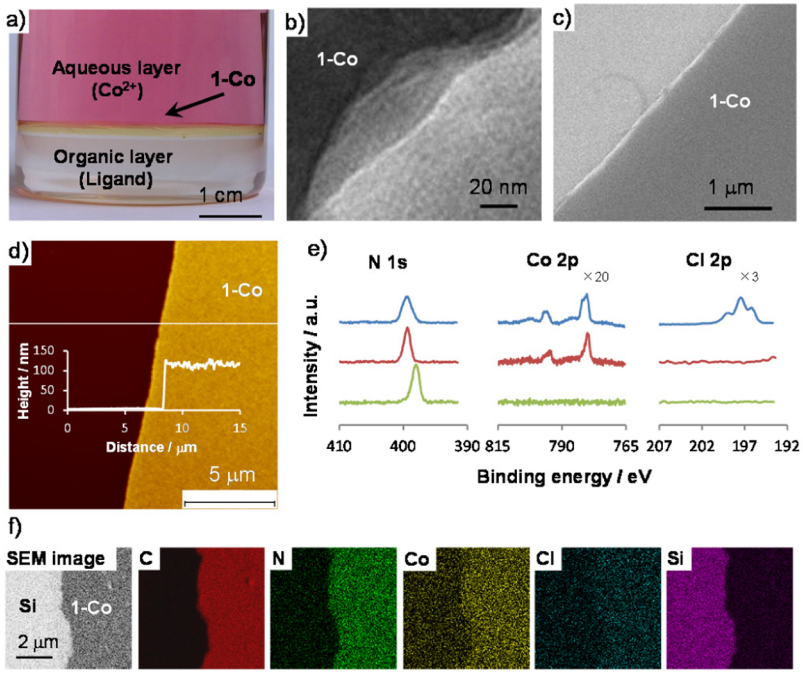

Figure 5. (a) **1-Co** generated at the liquid/liquid interface between 50 mM aqueous $CoCl_2$ and 0.1 mM **1** in $CHCl_3$ after 8 d. (b) TEM image of **1-Co**. (c) SEM image of **1-Co** deposited on a Si substrate. (d) AFM image and cross-sectional analysis of **1-Co** on a Si substrate. (e) XP spectra of **1** (green), mononuclear $[Co(tpy)_2](BF_4)_2{\cdot}H_2O$ (red), and **1-Co** (blue) focusing on N 1s, Co 2p, and Cl 2p core levels, respectively. The peak intensity is corrected using standard samples, thereby being proportional to the element abundance. (f) SEM/EDS mapping of **1-Fe** for C, N, Co, Cl, and Si.

We note that thinner **1-Co** (thickness: 10 nm, 6−7 layers) may be fabricated by diluting the aqueous phase to 25 mM and reducing the reaction time to 1 d (Figure S9). This demonstration also ensures the nanosheet nature of **1-Co**.

The chemical composition of **1-Co** was examined by XPS. XP spectra that focus on the N 1s, Co 2p, and Cl 2p regions of **1**, $[Co(tpy)_2](BF_4)_2{\cdot}H_2O$ (mononuclear complex), and **1-Co** are shown in Figure 5, panel e. The N 1s peak of **1-Co** (399.6 eV) appears in a higher binding energy region than that of ligand **1** (397.5 eV). This peak position is the same as that of the mononuclear complex (399.5 eV) and suggests that complexation occurred between Co^{2+} and the terpyridine ligand. No shoulder peak in the N 1s area means that the complexation is complete in **1-Co** as far as the quantitative detection limit of XPS is concerned (0.1−1 atom %). In the Co 2p region, the peak position of **1-Co** is the same as that of $[Co(tpy)_2](BF_4)_2{\cdot}H_2O$ (781.0 eV). This result also indicates the formation of the $[Co(tpy)_2]$ complex unit in **1-Co**. A peak derived from the counteranion, Cl^-, was also confirmed. Element abundance for **1-Co** was quantified using $[Co(tpy)_2](BF_4)_2{\cdot}H_2O$ and $CoCl_2$ as standard samples, which yielded N/Co/Cl = 5.86:1:2.13. This ratio is consistent with the ideal ratio (6:1:2), considering an accompanying error for XPS (10%). IR spectroscopy showed a shift in C=C stretching with the coordination (Figure S10). SEM/EDS mapping detected all constitutive elements of **1-Co** (C, N, Co, and Cl) that are located uniformly in the film (Figure 5f), manifesting the uniform composition of multilayer **1-Co**.

We also investigated the redox activity of **1-Co**. The $[Co(tpy)_2]^{2+}$ complex motif shows Co^{3+}/Co^{2+} and Co^{2+}/Co^{+} redox couples. Figure 6, panel a shows cyclic voltammogram of **1-Co** adsorbed on an ITO electrode. Two redox waves are visible at approximately −0.14 and −1.15 V, which are

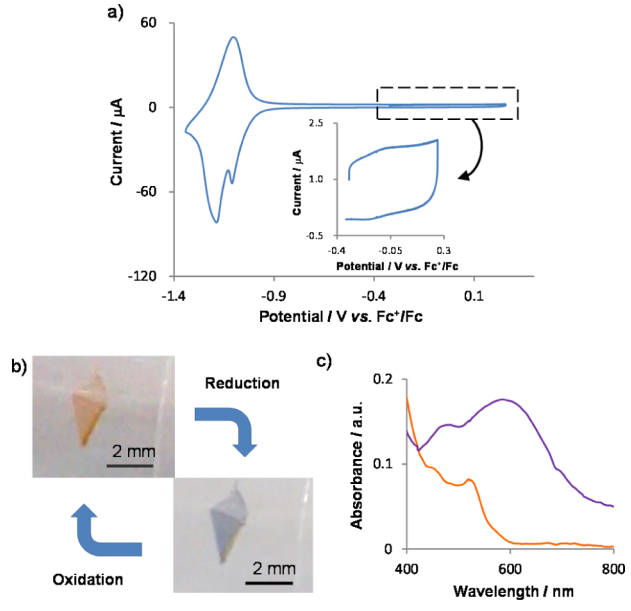

Figure 6. (a) Cyclic voltammograms of **1-Co** on ITO electrode in 1 M Bu_4NClO_4−CH_2Cl_2 solution (scan rate: 100 mV s^{-1}). (b) Electrochromism of **1-Co**. (c) UV−vis spectra of **1-Co** (orange) and reduced **1-Co** (purple).

assignable, respectively, to the Co^{3+}/Co^{2+} and Co^{2+}/Co^{+} couples. Again, these values are consistent with those of bis(terpyridine)cobalt complex wires.[28,29] The peak current for the former was much smaller than the latter, and in fact such a phenomenon is occasionally observed in cyclic voltammograms of $[Co(tpy)_2]$ coordination polymers.[29,34] This is associated with the slower electron transfer rate constant for the Co^{3+}/Co^{2+} couple than that for the Co^{2+}/Co^{+} couple: in fact, there is

DOI: 10.1021/ja510788b
J. Am. Chem. Soc. 2015, 137, 4681−4689

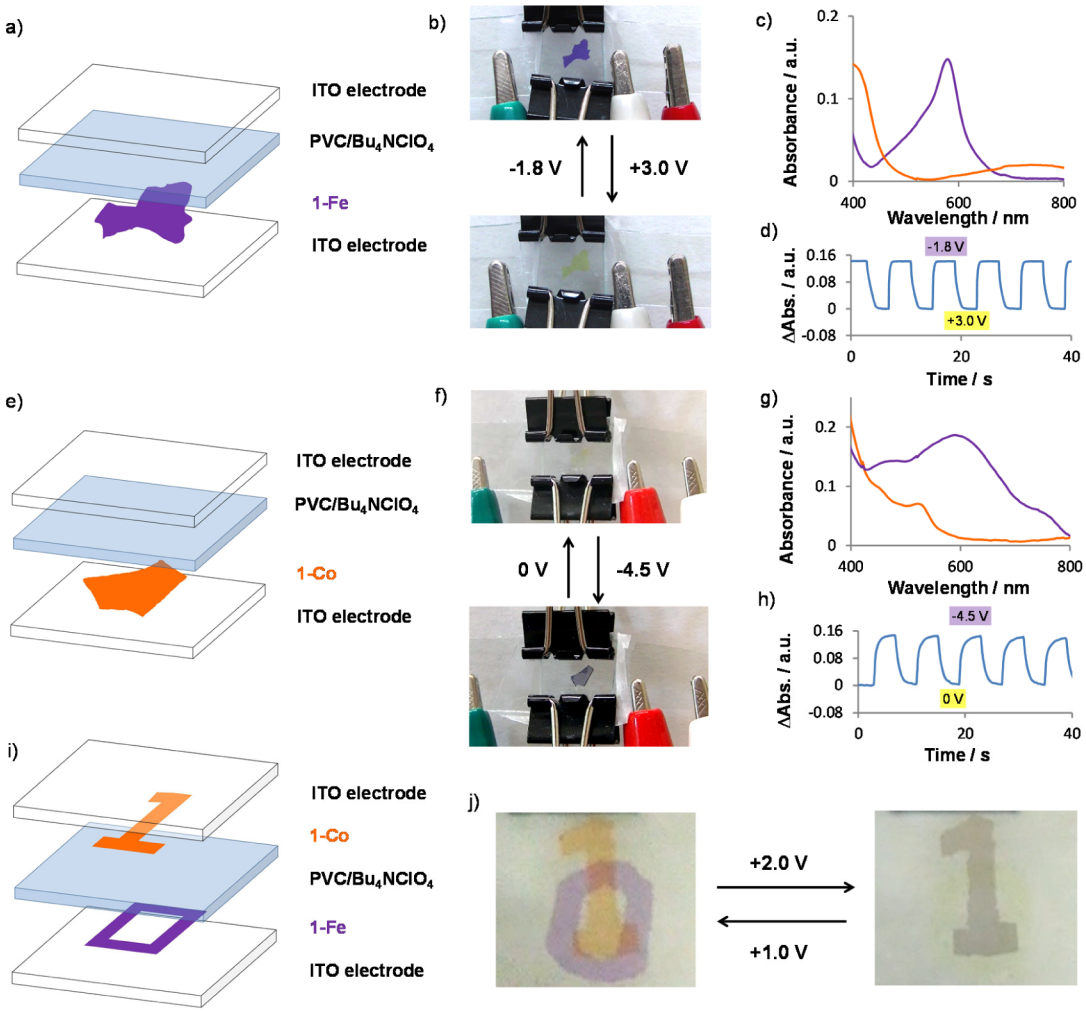

Figure 7. (a) Structure of electrochromic device composed of **1-Fe**. (b) Operation of the device with **1-Fe**. (c) UV−vis spectra of the device (orange, after oxidation at +3.0 V; purple, after rereduction at −1.8 V). (d) Spectral change at 579 nm during PSCA between +3.0 and −1.8 V. Each voltage was applied for 4 s. (e) Structure of electrochromic device composed of **1-Co**. (f) Electrochromic device with **1-Co**. (g) UV−vis spectra of the device with **1-Co** (purple, after reduction at −4.0 V; orange, after reoxidation at 0 V). (h) Change in absorbance at 600 nm during PSCA between −4.5 and 0 V. Each voltage was applied for 4 s. (i) Structure of dual-electrochromic device composed of **1-Fe** and **1-Co**. (j) Operation of the dual-electrochromic device with **1-Fe** and **1-Co**.

a very large discrepancy between their self-exchange electron transfer rate constants, 2 M^{-1} s^{-1} and 10^8 M^{-1} s^{-1}, respectively.[34] The subpeak in the Co^{2+}/Co^{+} redox wave is a contribution from charge trapping.[35]

By considering the cyclic voltammetry results, for electrochromism, we decided to exploit the Co^{2+}/Co^{+} redox couple that features more rapid electron transfer. Originally **1-Co** with the Co^{2+} center was orange (Figure 6b). Upon reduction to Co^{+} at −1.35 V, it changed to deep purple (Figure 6b and Movie 3 in the Supporting Information). When reduced **1-Co** was reoxidized to the Co^{2+} state, the nanosheet turned orange again. The absorption spectral change during the electrochemical measurement is shown in Figure 6, panel c. The reduction led to an increase at approximately 600 nm, which is also observed in a bis(terpyridine)cobalt(I) complex.[36]

Both iron and cobalt complex nanosheets with large domain sizes may be transferred onto substrates neat and tidy by using large reaction containers (Figure S1). Also, excellent thermal durability was confirmed by thermogravimetric analysis (Figure S11). Such demonstration and property may be appreciated by practical applications. We then fabricated a solid-state electrochromic system using a series of bis(terpyridine)metal complex nanosheets. The structure of the device is shown in Figure 7, panels a and e. Bu_4NClO_4-containing polyvinyl chloride was used as a solidified electrolyte.[37] The polymer electrolyte was sandwiched by a pair of ITO electrodes, on which **1-Fe** or **1-Co** was deposited (the ITO with nanosheet is regarded as a working electrode hereafter). Prior to electrochromism, we conducted cyclic voltammetry such that the redox reaction was active even in the solidified system (Figure S12). The device with **1-Fe** changed from deep purple to pale yellow at +3.0 V, and it recovered its original color at −1.8 V (Figure 7b and Movie 4 in the Supporting Information). The change in absorption spectrum of the device is summarized in Figure 7, panels c and d. The absorption peak at 579 nm disappeared with oxidation and was recovered reversibly with reduction. A solidified device using **1-Co** showed electrochromism from orange to deep purple with an applied voltage of −4.5 V. The voltage was changed to 0 V to induce the reoxidation of reduced **1-Co**, and a color recovery to orange was observed (Figure 7f and Movie 5 in the Supporting Information). The

DOI: 10.1021/ja510788b
J. Am. Chem. Soc. 2015, 137, 4681−4689

UV−vis spectral change during PSCA (Figure 7g,h) is similar to that measured in solution (Figure 6c).

Finally, we prepared a hybrid device that incorporated **1-Fe** and **1-Co**, thereby showing "dual" electrochromism. The configuration of the device is shown in Figure 7, panel i. One ITO electrode was modified with **1-Fe** (working electrode), whereas the other electrode with **1-Co** was regarded as a counter electrode. The nanosheets were cut into the numbers "0" and "1". In this device, the electrochemical reactions on the working and counter electrodes are identified (i.e., Fe^{3+}/Fe^{2+} and Co^{2+}/Co^{+}) so that unexpected and unidentified redox reactions on the counter electrode could be avoided. Figure 7, panel j and Movie 6 in the Supporting Information show that **1-Fe** and **1-Co** were oxidized and reduced simultaneously, respectively, when an external voltage of +2.0 V was applied. An external voltage of +1.0 V led to the rereduction and reoxidation of oxidized **1-Fe** and reduced **1-Co**, respectively. This series of redox reactions was accompanied by color changes, which highlighted 0 and 1 alternately.

■ CONCLUSIONS

We prepared submicron-thick bis(terpyridine)iron(II) or cobalt(II) complex nanosheets, **1-Fe**, **2-Fe**, and **1-Co**, by a liquid/liquid interfacial synthesis. The nanosheets were characterized using SEM, TEM, XPS, and UV−vis and IR spectroscopy, and their electrochemical properties were analyzed. The metal complex nanosheet was insoluble in any solvent but could be deposited easily onto various flat substrates. The nanosheet on an ITO electrode showed a fast, robust electrochromic response. A solidified electrochromic system was fabricated using the nanosheet, which suggests potential application in electrochemical devices such as color displays and electronic paper. We have achieved the hybridization of **1-Fe** and **1-Co** into one solid-state device to realize dual electrochromism.

■ EXPERIMENTAL SECTION

Materials. **1** and **2** were synthesized according the literature,[30,38] respectively. 2,2′:6′,2″-Terpyridine, $Fe(BF_4)_2{\cdot}6H_2O$, $Co(BF_4)_2{\cdot}6H_2O$, and $CoCl_2{\cdot}6H_2O$ were purchased from Tokyo Chemical Inc. or Aldrich and used without further purification. CH_2Cl_2 and MeCN were purchased from Kanto Chemical Co., Inc. and purified with Glass Contour Solvent Dispersing System (Nikko Hansen and Co., Ltd.). Acetone and ethanol were purchased from Kanto Chemical Co., Inc. and used without further purification. Water was purified with Milli-Q purification system (Merck KGaA). Tetra-*n*-butylammonium perchlorate was purchased from Tokyo Chemical Inc. and recrystallized from hot ethanol, then dried in vacuo.

Preparation of Substrates. Highly oriented pyrrolytic graphite was purchased from Alliance Biosystems, Inc. (Grade SPI-1 10 × 10 × 2 mm^3) and cleaved with an adhesive tape just before use. ITO−glass substrates were commercially available and washed under ultrasonication with following solvents successively: acetone (HPLC grade, 5 min ×2), pure water (5 min ×2), detergent solution, pure water (5 min ×3), then ethanol (HPLC grade, 10 min ×3). Si (111) wafer (P-type, B-doped, ≤ 0.005 Ω cm, E&M Corporation) was cut into small pieces and used as a Si substrate. As a substrate for SEM/EDS, a Si (111) wafer (n-type, P-doped, 0.03−0.04 Ω cm, E&M Corporation) was used. It was cut into small pieces and was immersed in a Piranha solution (120 °C, 10 min) to remove residual organic impurities on the surface.

Synthesis of 1-Fe. A 0.1 mM solution of **1** in CH_2Cl_2 was prepared by dissolving 1 mg of **1** into 10 mL of CH_2Cl_2, and the solution was filtrated prior to use. The solution was poured into a vial with a diameter of 40 mm, then pure water (10 mL) was allowed to cover the solution of **1** to form a water/oil interface.[25,40] An aqueous solution of $Fe(BF_4)_2$ (50 mM, 10 mL, filtrated before use) was then added to the water phase by slow pipetting. After 24 h, **1-Fe** emerged at the interface as a purple film. The aqueous layer was replaced with pure water, followed by the removal of both organic and aqueous phases. Ethanol and CH_2Cl_2 were added to **1-Fe**, which resulted in a suspension of **1-Fe** flakes. **1-Fe** was then collected by filtration and dried in vacuo.

Synthesis of 2-Fe. The same procedure as **1-Fe** was employed, except that a ligand **2** solution in CH_2Cl_2 (0.12 mM) was used instead of ligand **1**.

Synthesis of 1-Co. A 0.1 mM solution of **1** was prepared by dissolving 1 mg of **1** into 10 mL of $CHCl_3$, and the solution was filtrated before use. The solution was poured into a vial with a diameter of 40 mm, then pure water (10 mL) was allowed to cover the solution of **1** to form a water/oil interface. An aqueous solution of $CoCl_2$ (100 mM, 10 mL, filtrated before use) was added to the water phase by slow pipetting. After 8 d, **1-Co** emerged at the interface as an orange film. The aqueous layer was replaced with pure water, followed by the removal of both organic and aqueous phases. Ethanol and $CHCl_3$ were added to **1-Co**, which resulted in a suspension of **1-Co** flakes. **1-Co** was then collected by filtration and dried in vacuo.

Synthesis of $[Fe(tpy)_2](BF_4)_2{\cdot}H_2O$. In water (5.1 mL), 2,2′:6′,2″-terpyridine (40.4 mg, 173 μmol) and iron(II) tetrafluoroborate hexahydrate (28.7 mg, 85.0 μmol) were stirred for 2 h, then filtered. To the filtrate, an excess amount of ammonium tetrafluoroborate (1.46 g) in water (20 mL) was added, and precipitated purple solid was collected by filtration. The solid was washed with a small amount of water, then dried under vacuum. Yield 15.4 mg, 25.4%. Elemental analysis: found, C 50.25, H 3.59, N 11.33; calcd for $C_{30}H_{22}N_6FeB_2F_8{\cdot}H_2O$, C 50.46, H 3.39, N 11.77.

Synthesis of $[Co(tpy)_2](BF_4)_2{\cdot}H_2O$. In water (5.1 mL), 2,2′:6′,2″-terpyridine (42.6 mg, 183 μmol) and cobalt(II) tetrafluoroborate hexahydrate (30.6 mg, 84.3 μmol) were stirred for 2 h, then filtered. To the filtrate, an excess amount of ammonium tetrafluoroborate (1.52 g) was added, and precipitated brown solid was collected by filtration. The solid was washed with a small amount of water, then dried under vacuum. Yield 12.4 mg, 20.5%. Elemental analysis: found, C 50.15, H 3.62, N 11.38; calcd for $C_{30}H_{22}N_6CoB_2F_8{\cdot}H_2O$, C 50.25, H 3.62, N 11.72.

Transfer of the Nanosheets on Substrates. To transfer a small piece of the nanosheet onto a flat substrate (e.g., photographs in the manuscript except for Figure S1b), nanosheet flakes were redispersed in a mixture of CH_2Cl_2 and ethanol. The suspension was dropped onto a substrate using a pipet. After the solvent was evaporated, the modified substrate was dried with an Ar blow. On the other hand, to transfer a large piece of the nanosheet (e.g., Figure S1b), a substrate was placed at the bottom of the organic phase before constructing the liquid/liquid interfacial synthetic system. After the emergence of the nanosheet, both aqueous and organic phases were removed to allow the nanosheet to cover the substrate surface.

Characterization. TEM measurements were carried out with Hitachi HF2000 equipped with an AMT-CCD camera with an acceleration voltage of 75 kV. A suspension of the nanosheet flakes in CH_2Cl_2 and ethanol was dropped onto a copper grid or an elastic carbon grid and dried under vacuum overnight. FE-SEM images were recorded using JEOL JSM-7400FNT. The acceleration voltage was set to 15 kV. Samples for the FE-SEM observation was prepared by depositing **1-Fe** on an HOPG, and **2-Fe** and **1-Co** on Si substrates, respectively. SEM/EDS was measured on FEI Magellen 400L equipped with AMETKA/EDAX Genesis APEX4 operated at the acceleration voltage of 5 kV and 6 kV for the iron and cobalt nanosheets, respectively. XPS was measured using PHI 5000 Versa Probe (ULVAC-PHI). Al Kα (15 kV, 25 W or 20 kV, 100 W) was used as an X-ray source. The sample was deposited on a piece of a conductive carbon tape. The spectra were analyzed using a Multi Pak Software, and the binding energy was standardized using a C 1s peak at 284.6 eV. To quantify the element abundance of the nanosheet, $[Fe(tpy)_2](BF_4)_2{\cdot}H_2O$ was employed for **1-Fe** and **2-Fe**, whereas $[Co(tpy)_2](BF_4)_2{\cdot}H_2O$ and $CoCl_2$ were exploited for **1-Co** as standard

DOI: 10.1021/ja510788b
J. Am. Chem. Soc. 2015, 137, 4681−4689

samples. IR spectra were recorded using a JASCO FT/IR 620v spectrometer. All samples were pelletized with KBr (Wako Pure Chemical Industries, Ltd.). UV−vis spectra were obtained with a JASCO V570 spectrometer. AFM images were collected using an Agilent Technologies 5500 Scanning Probe Microscope. AFM was carried out using a silicon cantilever PPP-NCL or NCH (Nano World) in the high amplitude mode (Tapping Mode) under an ambient condition. The sample was prepared in the same way as that for the FE-SEM measurement. TGA was performed under a nitrogen atmosphere using Rigaku Thermo Plus2 TG8120. Al_2O_3 was used as a reference compound, and both nanosheet and Al_2O_3 were mounted on an Al pan. The temperature was controlled from r.t. to 500 °C with a scan rate of 10 °C s^{-1}.

Electrochemical Measurement. A series of electrochemical measurements was conducted using ALS 650B and ALS 650DT electrochemical analyzers. An HOPG substrate modified with **1-Fe** or **2-Fe** was used as a working electrode (0.264 cm^2), while a Pt was used as a counter electrode. A homemade Ag^+/Ag reference electrode (0.01 M $AgClO_4$ in 0.1 M Bu_4NClO_4/MeCN) was employed. On the other hand, **1-Co** was deposited on an ITO electrode, which was used as a working electrode. As a supporting electrolyte solution, 1 M Bu_4NClO_4 solution of CH_2Cl_2 or MeCN was used as a supporting electrolyte. For EIS, an ITO electrode (0.264 cm^2) modified with **1-Fe** or **2-Fe** was used as a working electrode. An AC potential centered at $E^{0\prime}$ was applied with an AC amplitude of 5 mV and frequencies spanning 0.01−100000 Hz. The fitting was implemented with a fitting program equipped in an ALS 650D software. The Randles circuit was adopted as an equivalent circuit.

Electrochromism. An ITO electrode modified with the nanosheet was employed as a working electrode, and counter and reference electrodes described above were used to construct a three electrode system. The movies and photographs were recorded on a GZ-HM980 camera (Victor Company of Japan, Ltd.). Spectroelectrochemical measurement was performed using a homemade electrochemical cell described in the literature.[39]

Preparation of Solid-State Electrochromic Devices. A PVC film (Toughnyl, 100 μm in thickness) was immersed into a 1 M Bu_4NClO_4 solution in 1,2-dichloroethane overnight. Then layered structures shown in Figure 7, panels a, e, and i were fabricated. "0" and "1" were engraved using a utility knife. The system was then dried overnight under an aerobic condition. The device was dried further for 2 h under vacuum, which was then subjected to a performance.

■ ASSOCIATED CONTENT

Supporting Information

SEM images, IR, UV−vis spectra, PSCA, EIS, TGA, and movies on the electrochromism and electrochromic devices. This material is available free of charge via the Internet at http://pubs.acs.org.

■ AUTHOR INFORMATION

Corresponding Author

*nisihara@chem.s.u-tokyo.ac.jp

Notes

The authors declare no competing financial interest.

■ ACKNOWLEDGMENTS

The authors acknowledge Grants-in-Aid from MEXT of Japan (Nos. 21108002, 24750054, 25107510, 26708005, 26107510, 26620039, 26220801, 26110505, areas 2107 [Coordination Programming], 2406 [All Nippon Artificial Photosynthesis Project for Living Earth], 2506 [Science of Atomic Layers], and 2509 (Molecular Architectonics)) and JSPS fellowship for young scientists. R.S. is grateful to Ogasawara Foundation for the Promotion of Science & Engineering, Noguchi Institute, Tokuyama Science Foundation, Asahi Glass Foundation, The Murata Science Foundation, Iketani Science and Technology Foundation, The Japan Prize Foundation, Kao Foundation for Arts and Sciences, Japan Association for Chemical Innovation, Iketani Science and Technology Foundation, The MIKIYA Science and Technology Foundation, Yazaki Memorial Foundation for Science and Technology, Shorai Foundation for Science and Technology, The Kurata Memorial Hitachi Science and Technology Foundation, and Kumagai Foundation for Science and Technology for financial supports. The authors acknowledge Dr. Koji Harano and Satoshi Okada (The University of Tokyo) for SEM/EDS, and Reserch Hub Advanced Nono Characterization (The University of Tokyo) for XPS.

■ REFERENCES

(1) Novoselov, K. S.; Geim, A. K.; Morozov, S. V.; Jiang, D.; Zhang, Y.; Dubonos, S. V.; Grigirieva, I. V.; Firsov, A. A. *Science* **2004**, *306*, 666.

(2) Bolotin, K. I.; Sikes, K. J.; Jiang, Z.; Klima, M.; Fudenberg, G.; Hone, J.; Kim, P.; Stormer, H. L. *Solid State Commun.* **2008**, *146*, 351.

(3) Dlubak, B.; Martin, M.-B.; Deranlot, C.; Servet, B.; Xavier, S.; Mattana, R.; Sprinkle, M.; Berger, C.; De Heer, W. A.; Petroff, F.; Anane, A.; Seneor, P.; Fert, A. *Nat. Phys.* **2012**, *8*, 557.

(4) Sasaki, T.; Watanabe, M.; Hashizume, H.; Yamada, H.; Nakagawa, H. *J. Am. Chem. Soc.* **1996**, *118*, 8329.

(5) Li, B.-W.; Osada, M.; Ozawa, T. C.; Ebina, Y.; Akatsuka, K.; Ma, R.; Funakubo, H.; Sasaki, T. *ACS Nano* **2010**, *4*, 6673.

(6) Umar, A.; Hahn, Y. B. *Nanotechnology* **2006**, *17*, 2174.

(7) Sakai, N.; Ebina, Y.; Takada, K.; Sakai, T. *J. Am. Chem. Soc.* **2004**, *126*, 5851.

(8) Etgar, L.; Gao, P.; Xue, Z.; Peng, Q.; Chandiran, A. K.; Liu, B.; Nazeeruddin, M. K.; Gratzel, M. *J. Am. Chem. Soc.* **2012**, *134*, 17396.

(9) Coleman, J. N.; et al. *Science* **2011**, *331*, 568.

(10) Lee, H. S.; Min, S.; Chang, Y.; Park, M. K.; Nam, T.; Kim, H.; Kim, J. H.; Ryu, S.; Im, S. *Nano Lett.* **2012**, *12*, 3695.

(11) Lee, H. S.; Min, S.-W.; Park, M. K.; Lee, Y. T.; Jeon, P. J.; Kim, J. H.; Ryu, S.; Im, S. *Small* **2012**, *8*, 3111.

(12) Zeng, Z.; Yin, Z.; Huang, X.; Li, H.; He, Q.; Lu, G.; Boey, F.; Zhang, H. *Angew. Chem., Int. Ed.* **2011**, *50*, 11093.

(13) Ma, R.; Liu, Z.; Li, L.; Iyi, N.; Sasaki, T. *J. Mater. Chem.* **2006**, *16*, 3809.

(14) Ma, R.; Liu, Z.; Takada, K.; Iyi, N.; Bando, Y.; Sasaki, T. *J. Am. Chem. Soc.* **2007**, *129*, 5257.

(15) Ida, S.; Shiga, D.; Koinuma, M.; Matsumoto, Y. *J. Am. Chem. Soc.* **2008**, *130*, 14038.

(16) Yan, D.; Lu, J.; Wei, M.; Han, J.; Ma, J.; Li, F.; Evans, D. G.; Duan, X. *Angew. Chem., Int. Ed.* **2009**, *48*, 3073.

(17) Yan, D.; Lu, J.; Ma, J.; Wei, M.; Evans, D. G.; Duan, X. *Angew. Chem., Int. Ed.* **2011**, *50*, 720.

(18) Bauer, T.; Zheng, Z.; Renn, A.; Enning, R.; Stemmer, A.; Sakamoto, J.; Schlüter, A. D. *Angew. Chem., Int. Ed.* **2011**, *50*, 7879.

(19) Zheng, Z.; Ruiz-Vargas, C. S.; Bauer, T.; Rossi, A.; Payamyar, P.; Sch ütz, A.; Stemmer, A.; Sakamoto, J.; Schlüter, A. D. *Macromol. Rapid Commun.* **2013**, *34*, 1670.

(20) Zheng, Z.; Opilik, L.; Schiffmann, F.; Liu, W.; Mergamini, G.; Ceroni, P.; Lee, L.-T.; Schütz, A.; Sakamoto, J.; Zenobi, R.; VandeVondele, J.; Schlüter, A. D. *J. Am. Chem. Soc.* **2014**, *136*, 6103.

(21) Chen, Y.; Li, M.; Payamyar, P.; Zheng, Z.; Sakamoto, J.; Schlüter, A. D. *ACS Macro Lett.* **2014**, *3*, 153.

(22) Makiura, R.; Motoyama, S.; Umemura, Y.; Yamanaka, H.; Sakata, O.; Kitagawa, H. *Nat. Mater.* **2010**, *9*, 565.

(23) Motoyama, S.; Makiura, R.; Sakata, O.; Kitagawa, H. *J. Am. Chem. Soc.* **2011**, *133*, 5640.

(24) Otsubo, K.; Haraguchi, T.; Sakata, O.; Fujiwara, A.; Kitagawa, H. *J. Am. Chem. Soc.* **2012**, *134*, 9605.

DOI: 10.1021/ja510788b
J. Am. Chem. Soc. 2015, 137, 4681−4689

(25) Kambe, T.; Sakamoto, R.; Hoshiko, K.; Takada, K.; Ryu, J.; Sasaki, S.; Kim, J.; Nakazato, K.; Takata, M.; Nishihara, H. *J. Am. Chem. Soc.* **2013**, *135*, 2462.
(26) Logacheva, N. M.; Baulin, V. E.; Tsivadze, A. Y.; Pyatova, E. N.; Ivanova, I. S.; Velikodny, Y. A.; Chernyshev, V. V. *Dalton Trans.* **2009**, 2482.
(27) Sakamoto, R.; Katagiri, S.; Maeda, H.; Nishihara, H. *Coord. Chem. Rev.* **2013**, *257*, 1493.
(28) Sakamoto, R.; Katagiri, S.; Maeda, H.; Nishimori, Y.; Miyashita, S.; Nishihara, H. *J. Am. Chem. Soc.* **2015**, *137*, 734.
(29) Kanaizuka, K.; Murata, M.; Nishimori, Y.; Mori, I.; Nishio, K.; Masuda, H.; Nishihara, H. *Chem. Lett.* **2005**, *34*, 534.
(30) Nishimori, Y.; Kanaizuka, K.; Murata, M.; Nishihara, H. *Chem.—Asian J.* **2007**, *2*, 367.
(31) Bhuvana, T.; Kim, B.; Yang, X.; Shin, H.; Kim, E. *Angew. Chem., Int. Ed.* **2013**, *52*, 1180.
(32) Puodziukynaite, E.; Oberst, J. L.; Dyer, A. L.; Reynolds, J. R. *J. Am. Chem. Soc.* **2012**, *134*, 968.
(33) (a) Han, F. S.; Higuchi, M.; Kurth, D. G. *J. Am. Chem. Soc.* **2008**, *130*, 2073. (b) Hu, C.-W.; Sato, T.; Zhang, J.; Moriyama, S.; Higuchi, M. *ACS Appl. Mater. Interfaces* **2014**, *6*, 9118.
(34) Guadalupe, A. R.; Usifer, D. A.; Potts, K. T.; Hurrell, H. C.; Mogstad, A.-E.; Abruña, H. D. *J. Am. Chem. Soc.* **1988**, *110*, 3462.
(35) Denisvich, P.; Willman, K. W.; Murray, R. W. *J. Am. Chem. Soc.* **1981**, *103*, 4727.
(36) Yoshida, T.; Iida, T.; Shirasagi, T.; Lin, R. J.; Kaneko, M. *J. Electroanal. Chem.* **1993**, *344*, 355.
(37) Nagashima, S.; Murata, M.; Nishihara, H. *Angew. Chem., Int. Ed.* **2006**, *45*, 4298.
(38) Cavazzini, M.; Quici, S.; Scalena, C.; Puntoriero, F.; Ganga, G. L.; Campagna, S. *Inorg. Chem.* **2009**, *48*, 8578.
(39) Namiki, K.; Sakamoto, A.; Murata, M.; Kume, S.; Nishihara, H. *Chem. Commun.* **2007**, 4650.
(40) Sakamoto, R.; Hoshiko, K.; Liu, Q.; Yagi, T.; Nagayama, T.; Kusaka, S.; Tsuchiya, M.; Kitagawa, Y.; Wong, W.-Y.; Nishihara, H. *Nat. Commun.* **2015**, *6*, 6713.

DOI: 10.1021/ja510788b
J. Am. Chem. Soc. 2015, 137, 4681−4689